

## Article

# Comparative Study of Larvicidal Activity of Spinel $\text{Co}_3\text{O}_4$ Nanorods and Entomopathogenic *Metarhizium brunneum* Conidia against *Culex pipiens*

Rania A. Mohamed<sup>1,\*</sup>, Wageha A. Mostafa<sup>2</sup>, Lamyaa M. Kassem<sup>3,\*</sup>, Niveen M. Ghazali<sup>4</sup> and Ahmed G. El-Shamy<sup>5</sup>

<sup>1</sup> Department of Biology, Deanship of Educational Services, Qassim University, P.O. Box 5888, Unaizah 56219, Saudi Arabia

<sup>2</sup> Entomology Section, Zoology Department, Faculty of Science, Zagazig University, Zagazig 44519, Egypt

<sup>3</sup> Department of Pharmacy Practice, Unaizah College of Pharmacy, Qassim University, P.O. Box 5888, Unaizah 51911, Saudi Arabia

<sup>4</sup> Department of Pharmaceutical Chemistry and Pharmacognosy, Unaizah College of Pharmacy, Qassim University, P.O. Box 5888, Unaizah 51911, Saudi Arabia

<sup>5</sup> Department of Physics, Faculty of Science, Suez Canal University, Ismailia 41522, Egypt

\* Correspondence: r.mohamed@qu.edu.sa (R.A.M.); l.mahmoud@qu.edu.sa (L.M.K.)

**Abstract:** Herein, we report the synthesis of spinel cobalt oxide nanorods ( $\text{Co}_3\text{O}_4$  NRs) by a modified co-precipitation approach and examine their larvicidal activity against *Culex pipiens*. The structure and morphology of the as-prepared  $\text{Co}_3\text{O}_4$  NRs were emphasized using X-ray diffraction (XRD), Raman spectroscopy, energy dispersive X-ray spectroscopy (EDAX), scanning electron microscopy (SEM), and transmission electron microscopy (TEM). It was found that  $\text{Co}_3\text{O}_4$  nanostructures have a face-centered spinel cubic crystal structure with a mean crystallite size of 38 nm. These nanostructures have a rod like shape with a mean diameter of 30 nm and an average length of 60 nm. The TGA measurements revealed the high stability of the formed spinel cubic structure at 400 °C. The optical behavior indicates the direct transition of electrons through an optical band gap in the range of 2.92–3.08 eV. These unique chemical and physical properties of  $\text{Co}_3\text{O}_4$  NRs enabled them to be employed as a strong agent for killing the *C. pipiens*. A comparison study was employed between the as-prepared  $\text{Co}_3\text{O}_4$  and the entomopathogenic fungus *Metarhizium brunneum* as a control agent of *C. pipiens* larvae. The results revealed that the as-prepared nanorods have higher mortality against *C. pipiens* larvae compared with the well-known *M. brunneum*.

**Keywords:** cobalt oxide ( $\text{Co}_3\text{O}_4$ ); nanorods; larvicidal; *Culex pipiens*; entomopathogenic fungi; *Metarhizium brunneum*



**Citation:** Mohamed, R.A.; Mostafa, W.A.; Kassem, L.M.; Ghazali, N.M.; El-Shamy, A.G. Comparative Study of Larvicidal Activity of Spinel  $\text{Co}_3\text{O}_4$  Nanorods and Entomopathogenic *Metarhizium brunneum* Conidia against *Culex pipiens*. *Molecules* **2022**, *27*, 7035. <https://doi.org/10.3390/molecules27207035>

Academic Editors: Qian Han, Nannan Liu, Qisheng Song and Jinsong Zhu

Received: 13 September 2022

Accepted: 14 October 2022

Published: 18 October 2022

**Publisher's Note:** MDPI stays neutral with regard to jurisdictional claims in published maps and institutional affiliations.



**Copyright:** © 2022 by the authors. Licensee MDPI, Basel, Switzerland. This article is an open access article distributed under the terms and conditions of the Creative Commons Attribution (CC BY) license (<https://creativecommons.org/licenses/by/4.0/>).

## 1. Introduction

Mosquitoes are responsible for the transmission of many parasites and pathogens that cause severe diseases, including lymphatic filariasis, Rift Valley Fever virus, yellow fever, malaria, and the Zika virus [1]. *C. pipiens* is the main vector of lymphatic filariasis disease (*Wuchereria bancrofti*), causing serious infection to millions of people annually [2]. Moreover, *Culex* spp. is a well-known primary source of annoyance for humans [3]. Recently, the scientific community has worked on using alternative strategies to the harmful chemical insecticide. In this regard, nanotechnology has been introduced as a safe and novel method to control mosquito species. The nanomaterials have gained significant attention from researchers owing to their distinctive physicochemical aspects and remarkable technological applications. In particular, transition metal oxides based nanoparticles of a semiconductor nature such as zinc oxide (ZnO), magnesium oxide (MgO), copper oxide (CuO), titanium dioxide ( $\text{TiO}_2$ ) and silver oxide ( $\text{Ag}_2\text{O}$ ) have been utilized in agriculture, pharmaceuticals, chemical engineering, and in the biomedical fields. For instance, cobalt oxide nanoparticles ( $\text{Co}_3\text{O}_4$  NPs) of high chemical reactivity, p-type semiconducting, and good magnetic

behavior were applied in medicine, supercapacitors, gas sensors, photocatalysis, and biological fields as an anticancer, antioxidant, and antimicrobial, with a small amount to overcome the relative toxic side effect [4–6]. Tu et al. (2022) have reported the antimicrobial, catalytic degradation activity, and biomedical effect of cobalt oxide nanosheets integrated with silver (Ag/Co<sub>3</sub>O<sub>4</sub>) [7]. Numerous routes have been developed for preparing the nanometal oxides such as sol gel, microwave-assisted reflux, co-precipitation, chemical vapor deposition, chemical spray pyrolysis, and a combustion approach [8,9]. Among the aforementioned techniques, chemical co-precipitation has attracted considerable attention because of its excellent features such as being cost effective, its simplicity in preparation, and its morphological well-defined structure. In the current study, the spinel cobalt oxide nanorods were synthesized by facile chemical approach for larvicidal activity against *C. pipiens*. In general, the nanoparticles can be found in different morphological shapes (i.e., nanosphere, nanoflake, nanocube, etc.) dependence of annealing temperature, electronegativity, and the pH of chemical reaction [10]. In the previous study, cobalt oxide NRs were functionalized as antimicrobials and a control agent for different types of mosquitoes owing to their large surface to volume area and surface plasmons [8,10]. On the other way, the use of entomopathogenic fungi (EPF) including *Metarhizium ansioptiae*, *M. brunneum*, and *Beauveria bassiana* as biocontrol agents attracted attention from health organizations based on their safety to human health and eco-friendly qualities compared with synthetic insecticides [11–13]. Moreover, the insect pathogenic fungus *Metarhizium* infects different developmental stages (eggs, larvae, and adults) of *Aedes*, *Anopheles*, and *Culex* mosquitoes, causing death [14,15]. EPF have a natural dispersal form known as conidia produced by conidiophores on the surface of the infected hosts. These conidia are resistant to desiccation and remain dormant in the soil for long periods, so they are commonly used for the control of agricultural pests [16]. Here, the strain of *M. brunneum* (petch 3826 CF Andrade) was applied to *C. pipiens* larval control that is characterized by the high yielding of pathogenic conidia [17]. The study revealed that the synthesized Co<sub>3</sub>O<sub>4</sub> nanorods performed better against *C. pipiens* compared with the utilized biological agent.

## 2. Materials and Methods

### 2.1. Chemicals

Cobalt chloride hexahydrate (CoCl<sub>2</sub>·6H<sub>2</sub>O), glutaraldehyde, cacodylate buffer, osmium tetroxide (OsO<sub>4</sub>), ethanol, acetone, and sodium hydroxide (NaOH) were purchased from Merck and the Alfa-Aesar Company.

### 2.2. Preparation Process

Cobalt oxide (Co<sub>3</sub>O<sub>4</sub>) was prepared by dissolving 3.45 g CoCl<sub>2</sub>·6H<sub>2</sub>O in 60 mL double distilled water under stirring at ambient temperature. Next, 30 mL NaOH solution was carefully added dropwise to the aqueous cobalt chloride with continuous stirring. The resulting precipitate was formed at pH monitored at 9. The powder was subsequently separated using filter paper and then washed many times with distilled water to remove the unreacted salts and residual ions. The product powder was dried in a furnace at 70 °C for 12 h and eventually annealed at 400 °C for 2 h.

### 2.3. Characterization of the Samples

The X-ray diffraction (XRD) (Model; Rigaku Smart Lab.) was carried out at wavelength 1.540 Å to investigate the crystal structure of cobalt oxide through the diffraction angle of 2θ range from 5°–80°. The phase content was recorded by Raman spectroscopy (Horiba Lab RAM HR Evolution). Scanning electron microscopy (SEM; Helios Nanolab. 400) and energy dispersive X-ray analysis (EDX) were examined to describe the surface topology and define the main elemental composition. Transmission electron microscopy (TEM, Hitachi-H-7500) worked at 100 kV was utilized to determine the mean size and particle distribution. Thermogravimetric (TGA, Netzsch Jupiter) was utilized under argon atmosphere to investigate the thermal stability of the nanoparticles. Cobalt oxide thin

film was deposited on glass substrates by a spin coater (SpinNXG-P1AC). UV-Vis optical absorbance was measured by a spectrophotometer (Jasco-V-570) for studying the optical properties of the thin film. The infected larvae were prefixed for 2 h in 2.5% glutaraldehyde and then rinsed in a 0.1 M cacodylate buffer (pH 7.2) for 15 min. It was then post-fixed for 1 h in 1% OsO<sub>4</sub> using the same buffer. The specimens were washed in buffer, dehydrated in an ethanol series, and treated in an acetone solution. After that, the specimens were coated with iridium for the SEM measurements. The mortality data were analyzed with SPSS version 14 using one-way analysis of variance (ANOVA) and Tukey's HSD tests for pair-wise comparisons. A probit transformation analysis was used to estimate the LC<sub>50</sub> at a 95% confidence limit of upper and lower values. The rate of mortality was corrected by Abbott's equation, [18] expressed as:

$$\text{Mortality (\%)} = \frac{T - C}{100 - C} \times 100 \quad (1)$$

where, T is the dead larvae in treatment, C is the dead larvae in control.

#### 2.4. Fungus Culture

The isolate *M. brunneum* patch 3826 CF Andrade (IF#1) was obtained from the Agriculture Research Service (ARSEF) in Ithaca New York (NY), USA. The fungus isolate was cultivated and maintained in a Sabouraud Dextrose Agar yeast (SDAY) medium. The plates were incubated at 28 °C for seven days. Over 2–3 weeks, the fungal culture was utilized to conduct various studies. Conidia were obtained by scraping the culture surface with a sterile loop in 10 mL distilled water. Tween 80 was added at a rate 0.1%. The spore suspension was filtered through a muslin cloth to eliminate mycelia. An upgraded Neubauer haemocytometer was used to calculate the spore count according to the literature [19].

#### 2.5. Mosquito Larval Culture

Larvae of *C. pipiens* were brought from Medical Entomology Institution, Cairo, Egypt. They were reared in a chamber insectary at 27 ± 2 °C, 70 ± 5% RH, and 14 L:10 D photoperiod. The adult mosquitoes were kept in cages (30 × 30 × 30 cm) and fed with 10% glucose solution. After a blood meal, the females laid eggs two days later. Egg rafts were gathered and stored in plastic bowls filled with water for hatching. Larvae were fed with commercial fish food (Shulet Carassius) and they were reared in white enamel dishes containing distilled water.

#### 2.6. Larvicidal Bioassay

The microbial control agent *M. brunneum* and chemical synthesized Co<sub>3</sub>O<sub>4</sub> NPs were separately examined against the third instar *C. pipiens* larvae. Firstly, five concentrations (1 × 10<sup>3</sup>, 1 × 10<sup>4</sup>, 1 × 10<sup>5</sup>, 1 × 10<sup>6</sup> and 1 × 10<sup>7</sup> spores/mL) of *M. brunneum* were applied. Conidia of each concentration were examined against *C. pipiens* larvae suspended in (0.1%) Tween-80. A group of larvae was treated in distilled water with Tween-80 (0.1%) as a control and by using pure distilled water as the negative control [20]. The NPs were evaluated at varied ratios ranging from 100 ppm to 600 Co<sub>3</sub>O<sub>4</sub> NPs [21], with minor alterations. For each case, larvae were divided into four replicates. Twenty larvae per replicate were transferred into 200 mL sterilized water in 250 mL plastic cups covered with mosquito netting. All cups were kept at 27 ± 2 °C, 70 ± 5% RH with a photoperiod of 14 L: 10 D. Mortality was observed daily for 96 h.

### 3. Results and Discussion

#### 3.1. Microstructural Analysis of Co<sub>3</sub>O<sub>4</sub> Nanorods

Figure 1 shows the XRD pattern of Co<sub>3</sub>O<sub>4</sub> NRs annealed at 400 C in air for 2 h. The spectrum exhibited a polycrystalline structure of weak crystallinity. The diffraction peaks detected at 2θ 19.07°, 31.40°, 37.02°, 38.80°, 44.95°, 55.61°, 59.46°, 65.32° according to the reflection planes (111), (220), (311), (222), (400), (422), (511), (440) belong to the face-centered

cubic phase of spinel  $\text{Co}_3\text{O}_4$  and match with the standard card (JCPDS No. 43-1003, space group  $\text{Fd}\bar{3}\text{m}$ ). No impurities or other phases related to unreacted salts or hydroxyl groups are observed in the pattern, suggesting the high purity of the compound [22]. For more structural analysis, the crystallographic parameters ( $D$ ,  $X_c$ ,  $\epsilon$ ,  $\delta$ ) were calculated from the XRD plot. The average crystallite size ( $D$ ) was defined using Debye's Scherrer formula by taking the full width at half maximum (FWHM) of the highest reflected peaks (311) and (440) [23]:

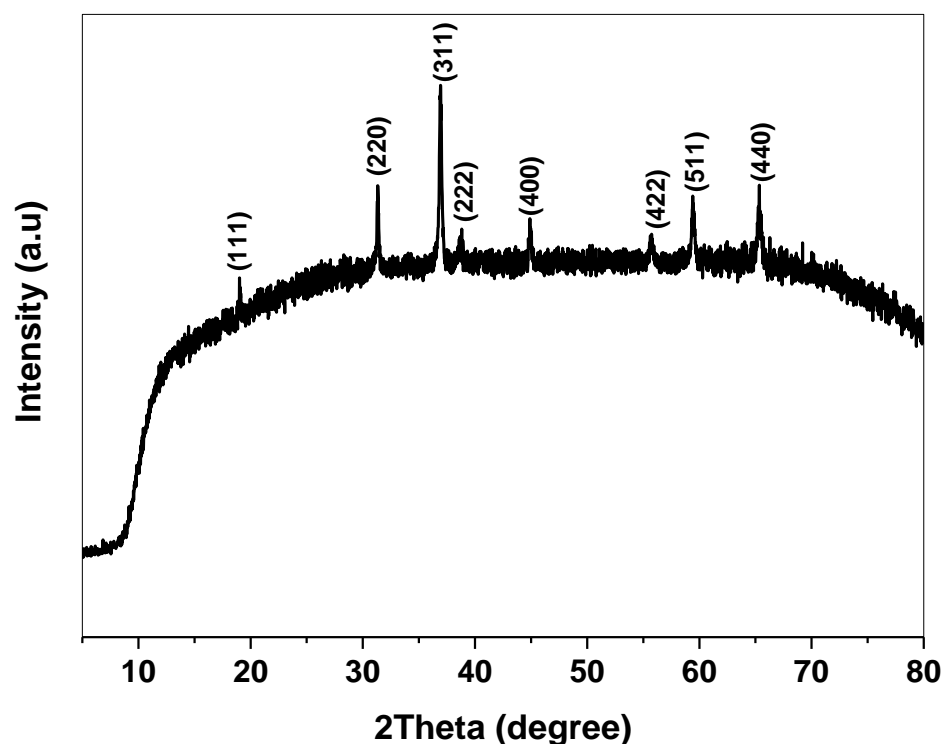


**Figure 1.** XRD pattern of the spinel  $\text{Co}_3\text{O}_4$  nanoparticles.

$D = \frac{k\lambda}{\beta \cos \theta}$ ;  $\beta$  is the line broadening at FWHM,  $k = 0.94$  is the shape factor, and  $\lambda$  is the wavelength of incident X-ray radiation = 1.540 Å. The degree of crystallinity ( $X_c$ ), lattice strain ( $\epsilon$ ), and dislocation density ( $\delta$ ) were also estimated using the equations [24]:

$X_c = \frac{0.24}{\beta}$ ,  $\epsilon = \frac{\beta}{4 \tan \theta}$ , and  $\delta = \frac{1}{D^2}$  lines/ $\text{m}^2$ , respectively. The summarized results in Table 1 revealed that  $\text{Co}_3\text{O}_4$  NPs of small crystallite size which is attributed to the large surface area. The particle size reduction and the good magnetic characteristics of spinel cobalt oxide allow it to easily penetrate the larval cuticle causing the toxic effect. Furthermore, the high values of the dislocation density ( $\delta$ ) and micro strain ( $\epsilon$ ) are associated with defects, atom disturbance, and the presence of the vacancies inside the cobalt oxide lattice.

**Table 1.** The crystallographic parameters of  $\text{Co}_3\text{O}_4$  NRs.

| The Nanoparticles       | Crystallographic Parameters |        |  |       |                           |
|-------------------------|-----------------------------|--------|--|-------|---------------------------|
|                         | FWHM                        | D (nm) | $\delta \times 10^{-4} (\text{nm})^{-2}$ | $X_c$ | $\epsilon \times 10^{-3}$ |
| $\text{Co}_3\text{O}_4$ | 0.23075                     | 38.00  | 7.00                                     | 59.55 | 12.00                     |

To define the molecular structure and phase content, a Raman spectrum was performed at room temperature through the wave number range of 150 to 800  $\text{cm}^{-1}$ . As illustrated in Figure 2a, there are four active Raman modes located at 667.17  $\text{cm}^{-1}$ , 506.14  $\text{cm}^{-1}$ , 462.75  $\text{cm}^{-1}$ , and 185.05  $\text{cm}^{-1}$  which clearly confirm the high quality of the prepared nanomaterial. The strongest peak located at wave number 667.17  $\text{cm}^{-1}$  is attributed to the  $\text{A}_{1g}$  phonon modes of the octahedral ( $\text{CoO}_6$ ) sites, whereas the peak at 186.976  $\text{cm}^{-1}$  is related to the tetrahedral ( $\text{CoO}_4$ ) sites [25]. The bands located at 506.14 and 462.75  $\text{cm}^{-1}$

are indexed to the second order Raman scattering resulting from phonons. The elemental chemical composition was recorded by EDX spectrum as illustrated in Figure 2b. The EDX spectrum of  $\text{Co}_3\text{O}_4$  is composed of cobalt (Co) and oxygen (O) elements with a weight percentage of 62.65 and 35.45 wt.%, respectively [10]. The peaks appeared at 0.277 keV and 1.978 keV were assigned to the carbon coated grid and an iridium coated sample was used for increasing its conductivity. No other undesired peaks were detected in the spectrum, which further confirms the high purity of the synthesized spinel compound. The surface morphology, design, and particle distribution were investigated by SEM and TEM spectroscopy. The SEM image (Figure 3a) that describes the surface of  $\text{Co}_3\text{O}_4$  is almost uniformly of sharp tiny rods with high density. Despite the large surface area, little pores were observed which may be related to lattice defects or the presence of vacancies [26,27]. The TEM micrograph described the particles in nanorod shapes of mean diameter  $\sim 30$  nm and mean length  $\sim 60$  nm (Figure 3b). Additionally, some of the particles are aggregated together due to the high surface energy and the size confinement effect [28,29].

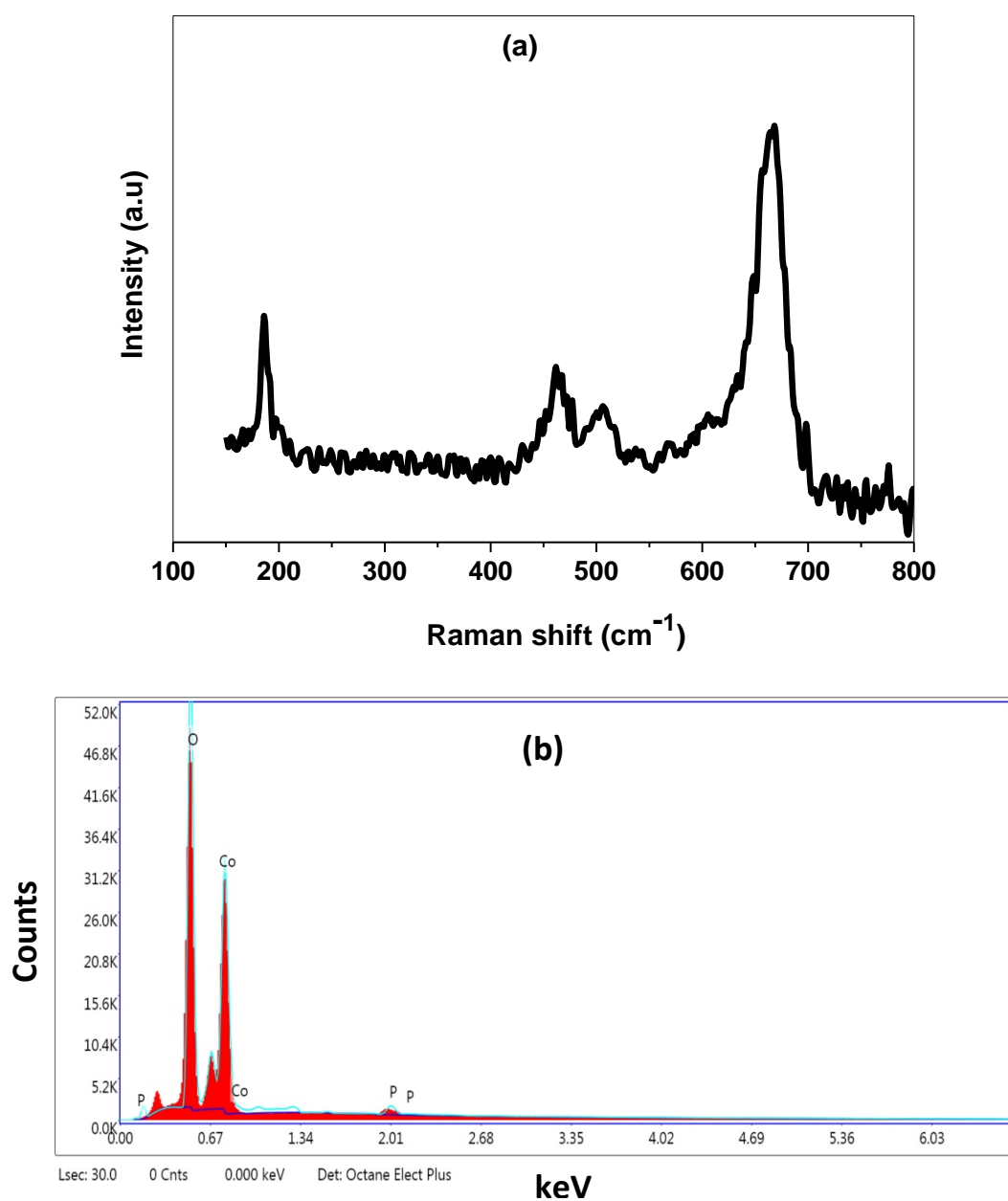


**Figure 2.** (a) Raman spectrum and (b) EDX spectrum of  $\text{Co}_3\text{O}_4$  nanoparticles.

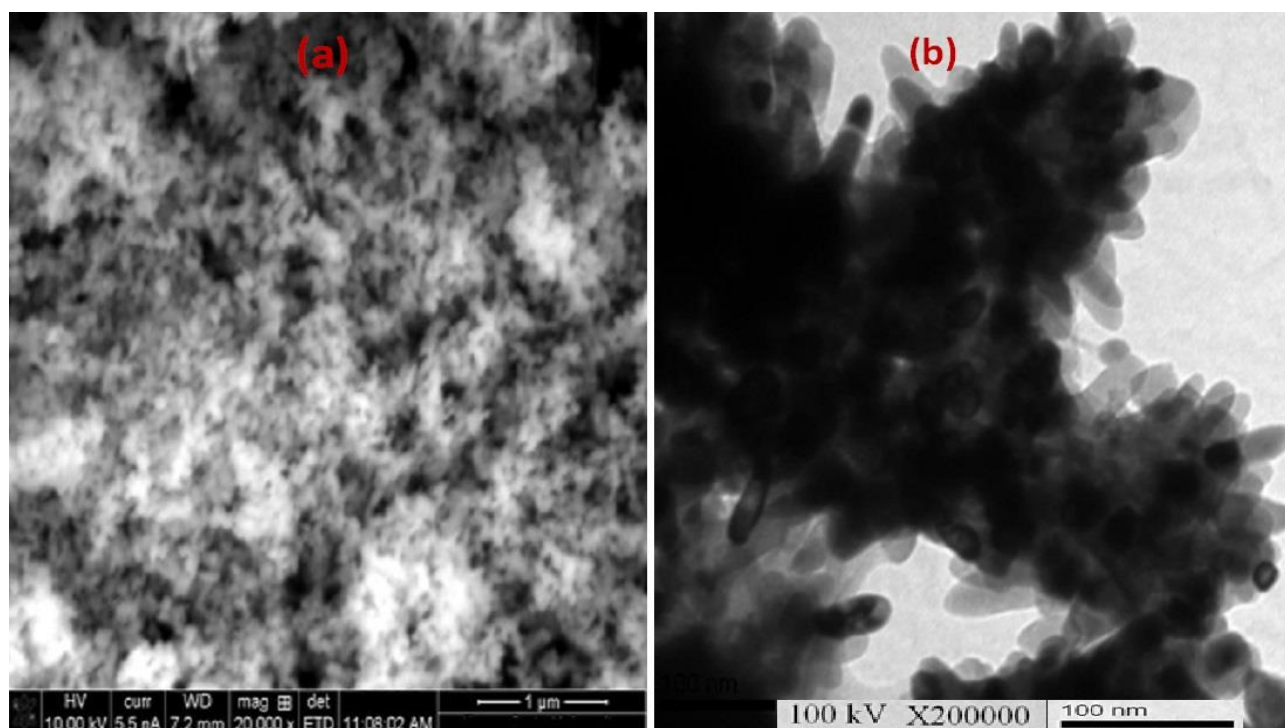


**Figure 3.** (a) SEM and (b) TEM micrographs of  $\text{Co}_3\text{O}_4$  nanorods.

### 3.2. Thermal and Optical Characteristics

The thermal properties of  $\text{Co}_3\text{O}_4$  NPs were analyzed by thermal gravimetric analysis (TGA) through the temperature range from 50–900 °C, as demonstrated in Figure 4. In the first stage, the weight loss through the temperature range 50–200 °C is the result of the evaporation of water molecules and absorbed moisture. In the second stage (300–400 °C), the TGA curve displayed the weight loss of hydroxyl decomposition and the removal of excess chemical salts. In the temperature range from 450 to 650 °C in the third stage, the spinel compound  $\text{Co}_3\text{O}_4$  showed thermal stability in which there was no loss of weight. In the last stage, up to 700 °C, the weight was suddenly lost, which may be owing to the phase transition [30].

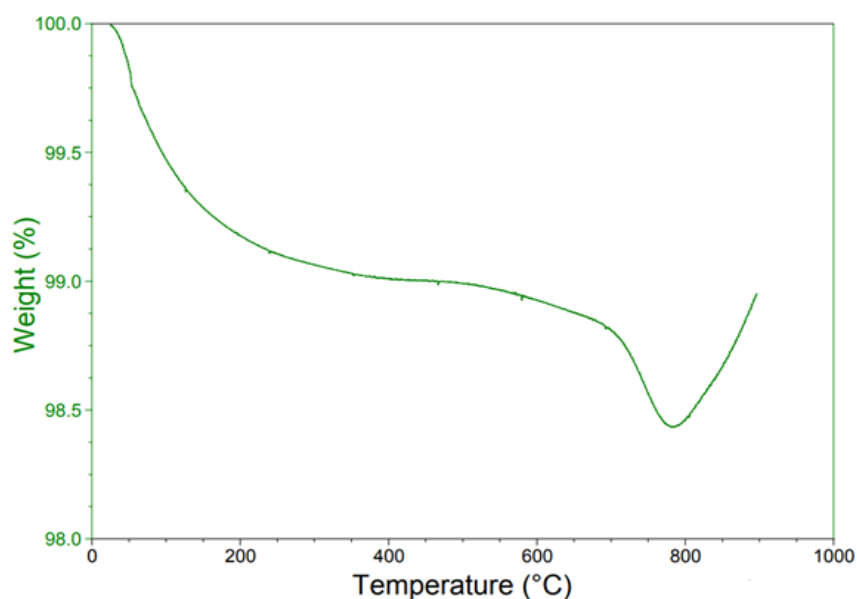


**Figure 4.** TGA curve of  $\text{Co}_3\text{O}_4$  nanoparticles.

The optical absorption of  $\text{Co}_3\text{O}_4$  thin films was measured within the UV-Vis region, as illustrated in Figure 5a. As can be seen, the spectrum has two absorption bands at 340 and 390 nm, revealing the broad light absorption and the strong interaction between the incident photon energy and the nanoparticles [31]. The presence of two sharp and weak bands is associated with structure disorder as well as generating new energy levels within the band gap. The energy gap ( $E_g$ ) is an important parameter which identifies the optical characteristics and the type of electron transition. The energy gap of the fabricated thin film was estimated from Tauc's formula, defined as [30]:

$$\alpha = \frac{A}{hv} (hv - E_g)^n \quad (2)$$

where,  $hv$  is the incident optical energy,  $A$  is the optical absorbance, and  $\alpha$  is the optical absorption coefficient expressed as [32,33]:

$$\alpha = \frac{2.303 A}{t} \quad (3)$$

$t$  is the thickness of the film. The  $E_g$  of  $\text{Co}_3\text{O}_4$  was evaluated by extending the straight line part of  $(\alpha hv)^2$  curve on the Y-axis to the energy on X-axis at  $(\alpha hv)^2 = 0$  (Figure 5b) exhibiting allowed direct transitions at 2.92 and 3.08 eV. The photon energy greater than the band gap means that more electrons transfer from to the conduction band and increase of free charge carriers [32,33].

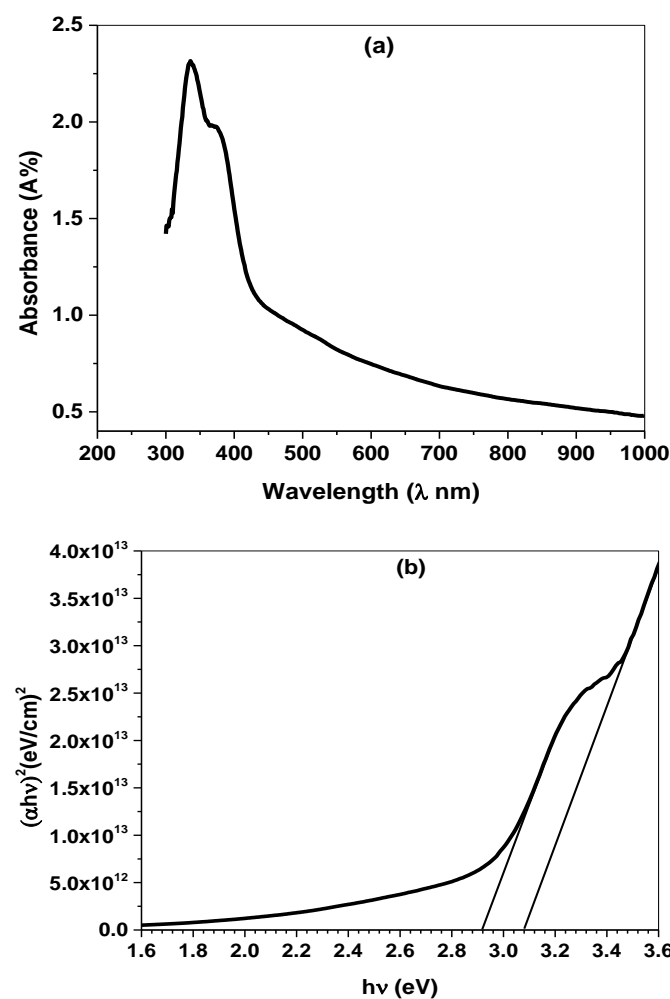


Figure 5. (a) Optical absorbance and (b) Energy gap of  $\text{Co}_3\text{O}_4$  thin film deposited on glass substrates.

### 3.3. The Larvicidal Performance of $\text{Co}_3\text{O}_4$ NPs

The larvicidal performance of  $\text{Co}_3\text{O}_4$  NPs against the third instar larvae of *C. pipiens* was examined. As presented in Table 2, the mortality rate was 100% at the ratio 600 ppm and  $30 \pm 0.478\%$  at 100 ppm. The difference in mortality at various NPs concentrations was statistically significant ( $F = 63.393$ ;  $df = 4$ ;  $p < 0.001$ ) and the  $\text{LC}_{50}$  value was 250.45 ppm. The probability analysis of *C. pipiens* larval mortality using the nanoparticles was illustrated in Figure 6b [34]. These results are consistent with Kainat et al. (2021) [35], who reported that  $\text{Co}_3\text{O}_4$  nanoparticles have larvicidal potential for *Aedes aegypti* with  $67.2 \pm 1.7\%$  mortality at 400 ppm compared with MgO NPs of  $49.2 \pm 8.1\%$  mortality at the same concentration. The impact of cobalt oxide nanoparticles on the treated larvae is a shape-dependent activity. The explanation for this is that when the nanoparticles interact with the body of mosquito larvae, spinel  $\text{Co}_3\text{O}_4$  dissociated into reactive oxygen species and released cobalt ions on the surface of the larvae [36,37]. The reactive oxygen species cause oxidative stress and lipid peroxidation, which inhibits larval growth [38]. Furthermore, nanorods provided an effective direct path for carriers that easily penetrated the mosquito cells leading to larval death [39].

**Table 2.** Toxic effect of fungus, *M. brunneum*, and  $\text{Co}_3\text{O}_4$  NPs against 3rd larval instar of *C. pipiens*.

| Test Samples                | Conc.           | % Mortality Percentage,<br>Mean $\pm$ SE | $\text{LC}_{50}$<br>(LCL–UCL)  | Regression Equation            | $\chi^2$ |
|-----------------------------|-----------------|--|--|--------------------------------|----------|
| $\text{Co}_3\text{O}_4$     | ppm             |  | 250.45<br>(209.20:285.72 ppm)  | $Y = -0.97 + (X \times 0.007)$ | 0.201    |
|                             | 100             | $30 \pm 0.478$                           |  |                                |          |
|                             | 200             | $45 \pm 0.250$                           |  |                                |          |
|                             | 300             | $57 \pm 0.478$                           |  |                                |          |
|                             | 400             | $68 \pm 1.080$                           |  |                                |          |
|                             | 500             | $79 \pm 0.250$                           |  |                                |          |
| 600                         | $100 \pm 0.00$  |  |  |                                |          |
| <i>Metarhizium brunneum</i> | spores/mL       |  | $1.3 \times 10^3$<br>( $5.86 \times 10^2$ : $2.31 \times 10^3$<br>spores/mL) | $Y = -51.5 + (X \times 0.5)$   | 0.906    |
|                             | $1 \times 10^3$ | $50 \pm 0.816$                           |  |                                |          |
|                             | $1 \times 10^4$ | $65 \pm 0.707$                           |  |                                |          |
|                             | $1 \times 10^5$ | $78.75 \pm 0.629$                        |  |                                |          |
|                             | $1 \times 10^6$ | $90 \pm 0.707$                           |  |                                |          |
|                             | $1 \times 10^7$ | $97.5 \pm 0.288$                         |  |                                |          |

$\text{LC}_{50}$ : lethal concentration that kills 50% of the exposed *C. pipiens* larvae; UCL: upper confidence limit; LCL: lower confidence limit;  $\chi^2$  = Chi-square,  $p < 0.05$ , significance level, Mean value of five replicates, (SE) standard error. Control (distilled water), nil mortality.

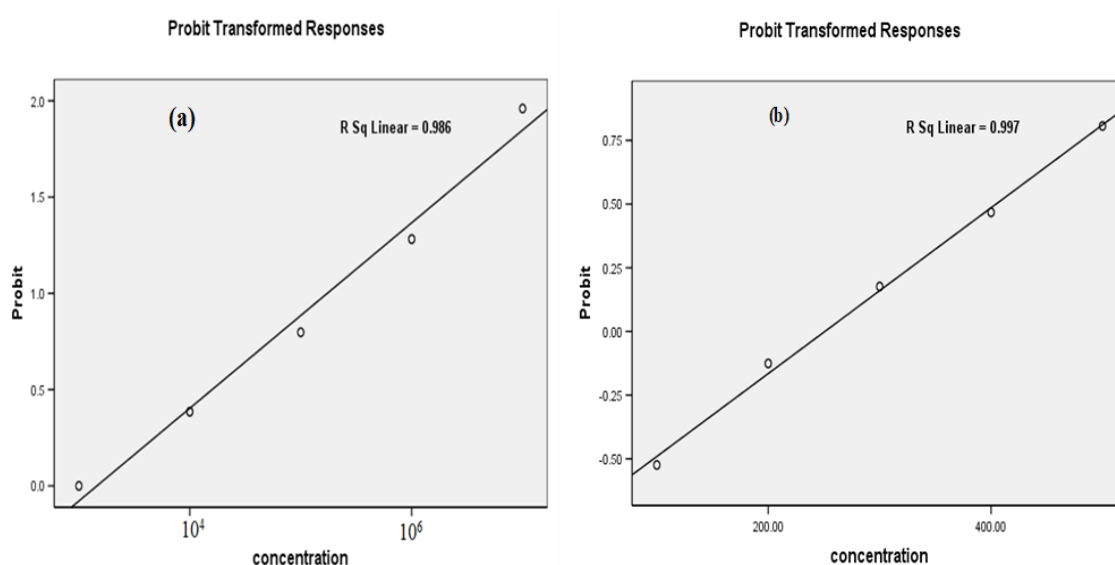


**Figure 6.** (a,b) The probability analysis of mortality of *C. pipiens* mosquito larvae by fungus, *M. brunneum* and  $\text{Co}_3\text{O}_4$  NPs.

A SEM observation showed that  $\text{Co}_3\text{O}_4$  nanorods concentrated on the body surface of the treated larvae (Figure 7). Damage in the head region and accumulation of NPs in the mouth brushes were demonstrated in Figure 7a,b. Also, Figure 7c,d illustrated the high density of  $\text{Co}_3\text{O}_4$  NPs on the thoracic area, especially between the inter-segment, while Figure 8a,b showed deformation of the abdomen cuticle, which is the reason for the rupture of the cuticle wax layer and causes the malfunction of this layer, leading to insect dehydration and finally death. Moreover, the particles were concentrated in the gills and respiratory siphon, causing suffocation, as seen in Figure 8c,d. The toxicity of NPs against mosquito larval instars is related to their ability to penetrate through the exoskeleton, according to earlier studies on mosquito larvae [40–42]; when the nanostructure material enters the intracellular space, they bind to sulfur from proteins which leads to the rapid denaturation of organelles. Additionally, the loose membrane permeability and loss of cellular function leads to cell death [43,44].

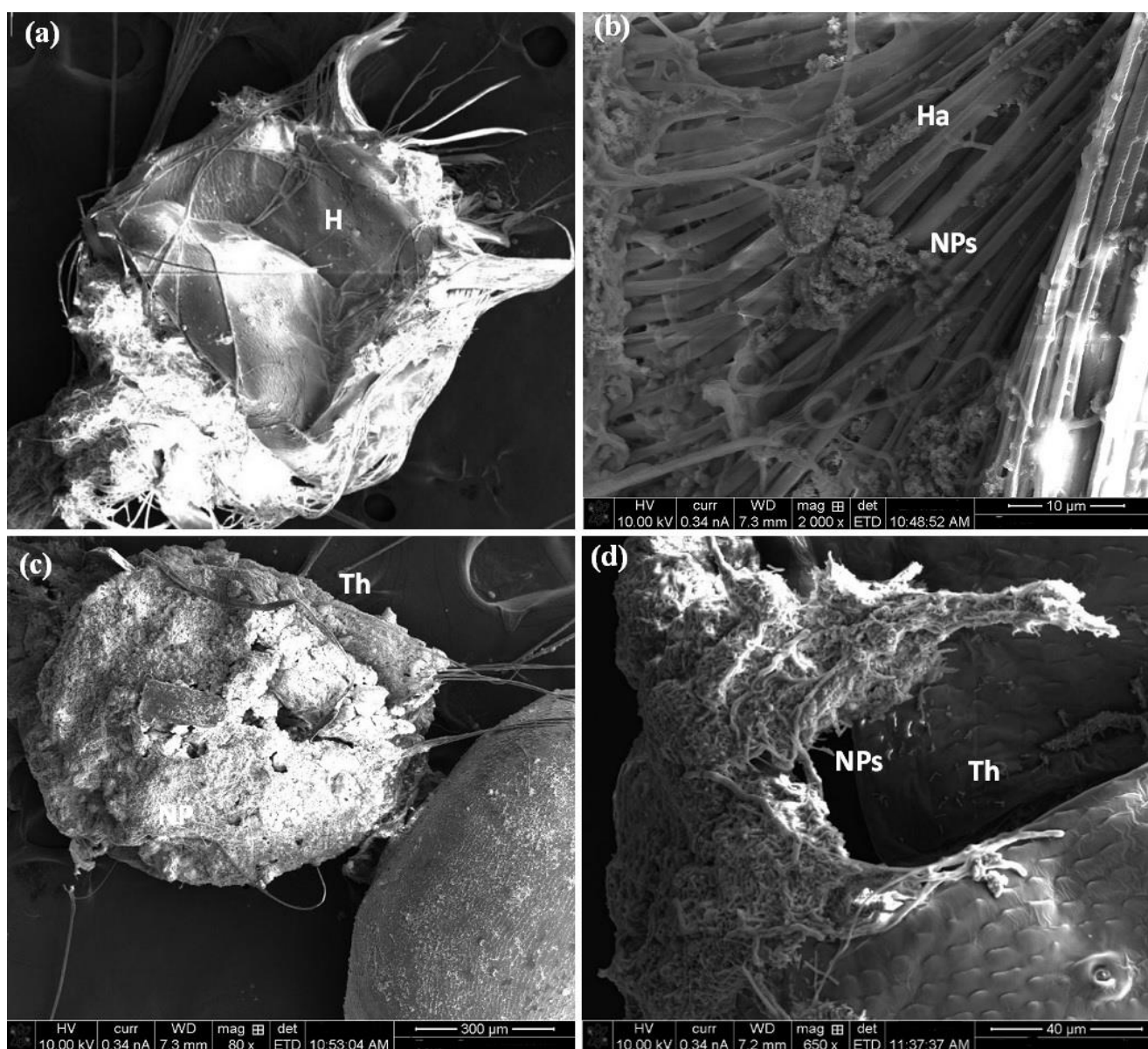


**Figure 7.** SEM of *C. pipiens* (body parts) exposed to  $\text{Co}_3\text{O}_4$  NPs. (a,b) show that  $\text{Co}_3\text{O}_4$  adheres to the head region and mouth parts. (c,d) display the NPs attached to the thoracic cuticle. (Th: thoracic, Cu: cuticle, H: head, Ha: head hair, Mp: mouthparts, NPs: nanoparticles).

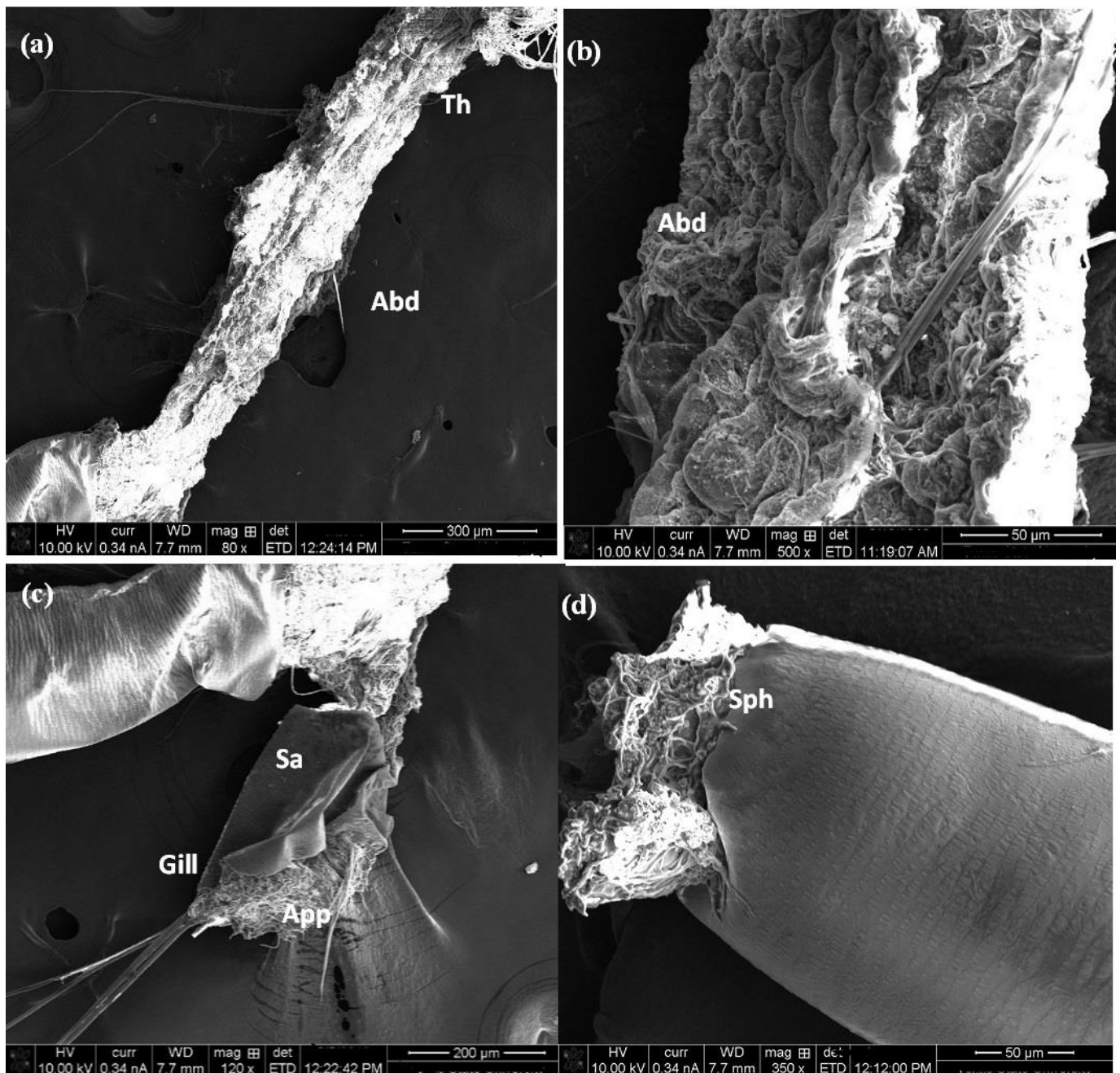


**Figure 8.** SEM of *C. pipiens* (body parts) exposed to  $\text{Co}_3\text{O}_4$  NPs. (a,b) show that  $\text{Co}_3\text{O}_4$  adheres to the abdominal cuticle. (c,d) demonstrate the NPs in the respiratory siphon and gills. (Abd: Abdomen, Cu: cuticle, G: gill, Sa: saddle, Siph; siphon).

### 3.4. Entomopathogenic Fungus Infection

The exposure of the third larval instar of *C. pipiens* to fungus (*M. brunneum*) described in Figure 9a, b revealed larvicidal activity. The treatment of *M. brunneum* demonstrated a significant larval mortality, where, the highest spore concentration ( $1 \times 10^7$ ) was recorded at larval mortality rates up to  $97.5 \pm 0.288\%$  at 96 h, while the mortality rate was  $50 \pm 0.816$  at low concentrations. Moreover, the difference in the rates of larval mortality at different concentrations were statistically significant ( $F = 34.078$ ;  $df = 4$ ;  $p < 0.000$ ) with  $\text{LC}_{50}$  value  $1.3 \times 10^3$  spores/mL (Table 2). The probability analysis of *C. pipiens* larval mortality was illustrated in Figure 6a. The obtained results confirmed that the conidia of the pathogenic terrestrial fungus, *M. brunneum*, has a strong virulence against the larval stage of *C. pipiens*,

specifically at the highest concentration. Entomopathogenic fungi have the ability to attack and invade aquatic mosquito stages [45,46]. Other studies show that the conidia of *M. anisopliae* strains are pathogenic against *Aedes*, *Anopheles*, and *Culex* larvae, and other vectors such as midges and ticks [17,47]. Alkhaibari et al. [48] have reported the positive impact of *M. brunneum* against *C. pipiens* larvae. Additionally, *C. quinquefasciatus* larvae were more susceptible to *M. brunneum* conidia infection than blastospore infection due to the larval instars of *C. quinquefasciatus* having a stronger and faster defense reaction to blastospores than conidia [48]. The study showed that the presence of *Culex* larvae close to the water surface expose them to a great amount of hydrophobic conidia [49].

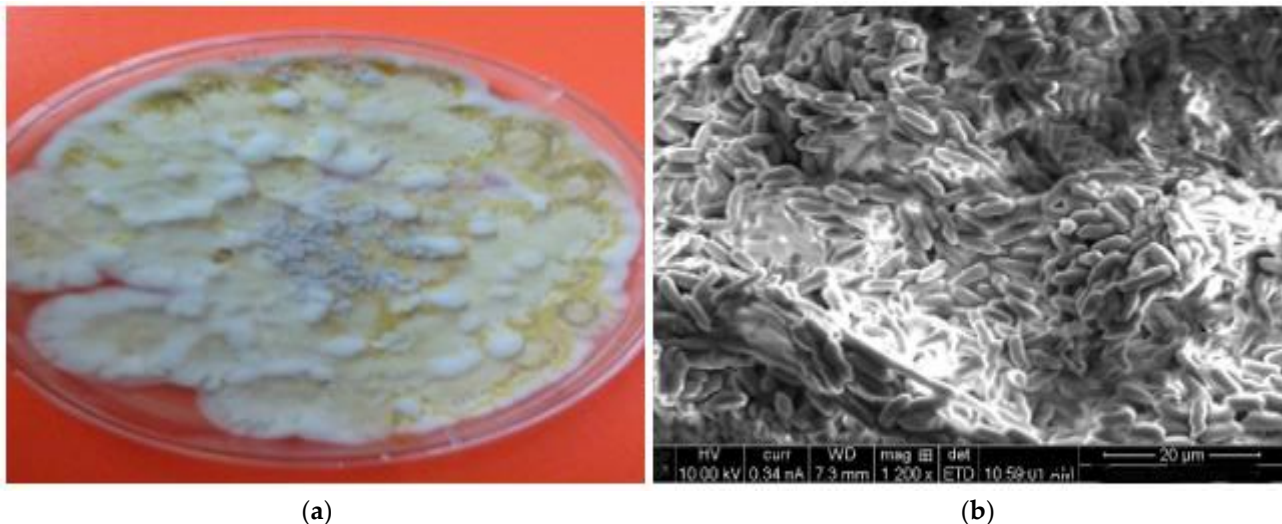


**Figure 9.** (a) Colony growth of *M. brunneum* on SAB media after 14 days of incubation at 27 °C and (b) SEM of the fungus culture.

In the SEM micrograph observation, infected larvae showed that the fungal spores of *M. brunneum* are attached to the surface of the larval cuticle of *C. pipiens* at various body parts (Figure 10) at 48 h post-treatment. These conidia stuck to the head hair (Figure 10a,b). In addition, the fungus' mycelium penetrated the abdomen cuticle (Figure 10c,d). Moreover, conidia penetrated and germinated in the siphon and gills leading to blocking the respiratory opening and larval suffocation (Figure 10e,f). These observations were coincident with Alkhaibari et al. [45], who revealed that *M. brunneum* blastospores adhered to the *Aedes aegypti* cuticle surface 24 h after treatment. Furthermore, conidia adhesion to *C. quinquefasciatus* larvae was shown to be higher on the siphon and head areas, particularly around the mouthparts [15]. Furthermore, hydrophobic lipids in the external epicuticular wax layer can play a vital role in the attachment and germination of fungal propagules [50]. Fungi with hydrophobic conidia allow hyphal growth into the tracheal system causing suffocation to the host and leading to its death [51]. Previous studies investigate the histopathological influence of entomopathogenic fungi on different insect structures, which indicated that the most relevant site of fungal attachment is the insect cuticle [44]. EPF exhibit their effect on the insect cuticle both mechanically, by penetration, as well as through chemical lysis of the cuticle and the whole body tissues by the action of chitinase, protease, and lipase enzymes [52].

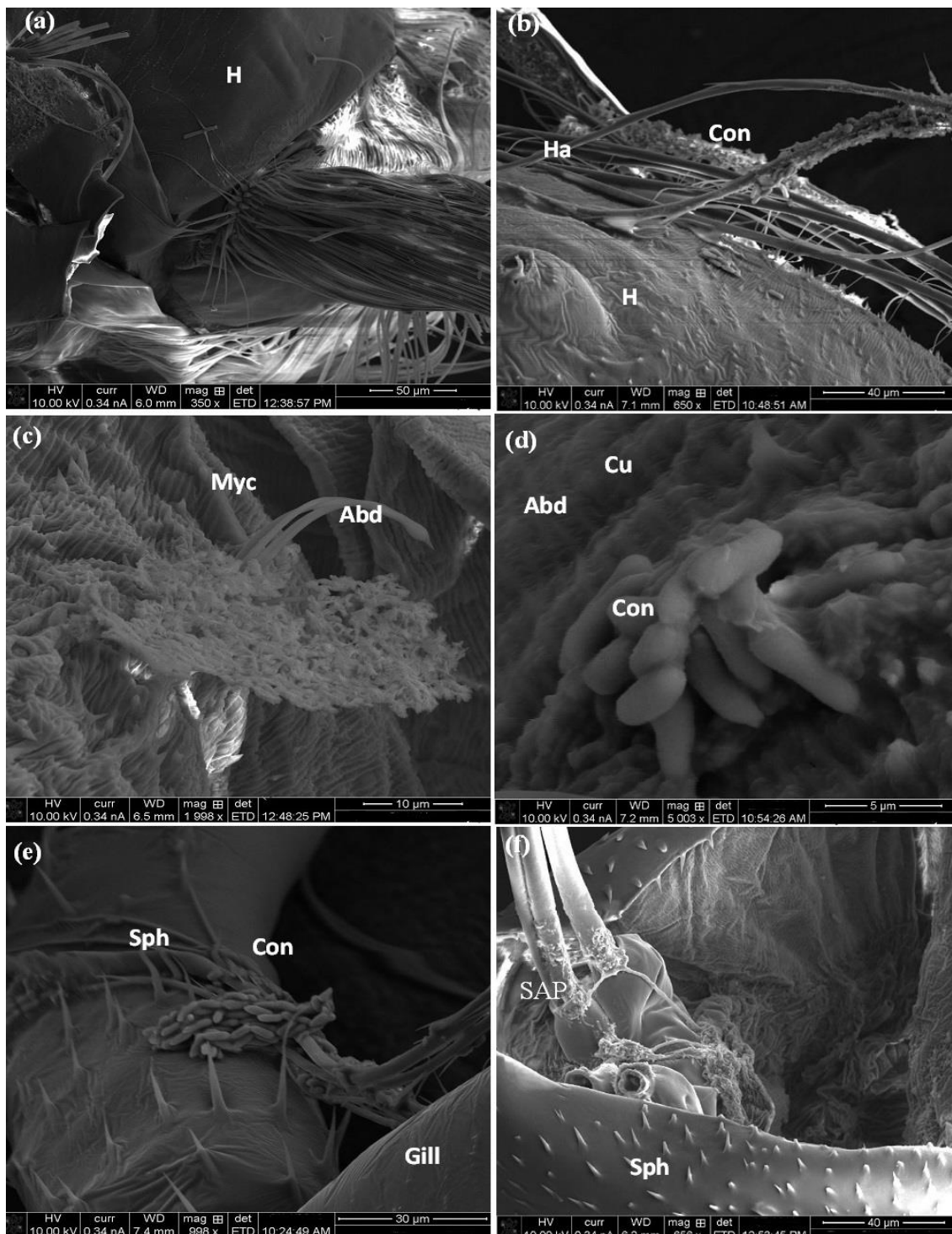


**Figure 10.** SEM of larval body surface (head, abdomen, and respiratory siphon, gills) of *C. pipiens* treated with fungus, *M. brunneum*. (a,b) *M. brunneum* adheres to the hair of the head. (c,d) attachment of *M. brunneum* to the abdominal cuticle and (e,f) to the respiratory system. (Abd: Abdomen, Co: conidia, Cu: cuticle, Gill: gills, H: head, Ha: head hair, Siph: siphon, SAP: spiracular apparatus).

To elucidate whether the effect of  $\text{Co}_3\text{O}_4$  nanorods is beneficial as an effective larvicidal nanomaterial, we compared the synthesized nanorods results with the fungus. The mortality rates were estimated to be 100% for NRs and 97.5% for the fungus. Therefore, the  $\text{Co}_3\text{O}_4$  NRs were more effective in the control of mosquito larvae.

#### 4. Conclusions

Spinel cobalt oxide nanorods with aspect ratio (length/diameter = 2) were successfully prepared by a simple chemical approach. These nanorods showed high thermal stability and optical band gap within the visible region (2.98–3.08 eV). These unique properties enabled the as-prepared cobalt oxide to be used as an efficient agent against *C. pipiens*. The results confirmed that the nanorods have the ability to get rid of all of the larvae with high efficiency compared to the fungus. Therefore, one may conclude that a new strong agent based on  $\text{Co}_3\text{O}_4$  NRs was developed to suppress mosquito larvae.

**Author Contributions:** R.A.M., W.A.M., L.M.K., N.M.G. and A.G.E.-S. contributed equally. All authors have read and agreed to the published version of the manuscript.

**Funding:** The authors extend their appreciation to the Deputyship for Research & Innovation, Ministry of Education, Saudi Arabia for funding this research work through the project number (QU-IF-05-01-28626). The authors also thank to Qassim University for Technical support.

**Institutional Review Board Statement:** Not applicable.

**Informed Consent Statement:** Not applicable.

**Data Availability Statement:** Not applicable.

**Conflicts of Interest:** The authors declare no conflict of interest.

**Sample Availability:** Samples of the compounds are available from the authors.

#### References

1. WHO. World Health Organization, Vectors Borne Diseases. 2020. Available online: <https://www.who.int/newsroom/factsheets/detail/vector-borne-diseases> (accessed on 14 April 2022).
2. Hamama, H.M.; Zyaan, O.H.; Ali, O.A.; Saleh, D.I.; El-Akkad, H.A.; El-Saadony, M.T.; Farag, S.M. Virulence of entomopathogenic fungi against *Culex pipiens*: Impact on biomolecules availability and life table parameters. *Saudi J. Biol. Sci.* **2022**, *29*, 385–393. [CrossRef] [PubMed]
3. Hesson, J.C.; Schäfer, M.; Lundström, J.O. First report on human-biting *Culex pipiens* in Sweden. *Parasites Vectors* **2016**, *9*, 632. [CrossRef] [PubMed]
4. Khalil, A.T.; Ovais, M.; Ullah, I.; Ali, M.; Shinwari, Z.K.; Maaza, M. Physical properties, biological applications and biocompatibility studies on biosynthesized single phase cobalt oxide nanoparticles via *Sageretia thea*. *Arab. J. Chem.* **2017**, *13*, 606–619. [CrossRef]
5. Sundar, L.S.; Singh, M.K.; Pereira, M.B.; Sousa, A.C.M. *The Cobalt Oxide-Based Composite Nanomaterial Synthesis and Its Biomedical and Engineering Applications*, (Book Chapter-Cobalt and Its Compounds); IntechOpen: London, UK, 2019; pp. 1–20.
6. Cai, Z.; Bi, Y.; Hu, E.; Liu, W.; Dwarica, N.; Tian, Y.; Li, X.; Kuang, Y.; Li, Y.; Yang, X.Q.; et al. Single-crystalline ultrathin  $\text{Co}_3\text{O}_4$  nanosheets with massive vacancy defects for enhanced electrocatalysis. *Adv. Energy Mater.* **2018**, *8*, 1–8. [CrossRef]
7. Tu, W.; Cheng, J.; Yang, R.; Guo, Z.; Yu, D.; Sheng, Z.; Zhao, J.; Song, H.; Song, Y.; Yang, F. The  $\text{Co}_3\text{O}_4$  nanosheet hybridized with silver nanoparticles affords long-acting synergistic antimicrobial and catalytic degradation activity. *J. Alloy. Compd.* **2022**, *419*, 165284. [CrossRef]
8. Jansirani, B.; Shilpa, P.; Raj, B.; Kumar, S. Controlled synthesis and electrochemical properties of Ag-doped  $\text{Co}_3\text{O}_4$  nanorods. *Int. J. Hydrog. Energy* **2017**, *42*, 29666–29671.
9. Allaedi, G.; Muhammad, A. Study of influential factors in synthesis and characterization of cobalt oxide nanoparticles. *J. Nanostruct. Chem.* **2013**, *3*, 1–16.
10. Naveen, A.N.; Selladurai, S. Tailoring structural, optical and magnetic properties of spinel type cobalt oxide ( $\text{Co}_3\text{O}_4$ ) by manganese doping. *Phys. B Condens. Matter* **2015**, *457*, 251–262. [CrossRef]
11. Vivekanandhan, P.; Swathy, K.; Murugan, A.C.; Krutmuang, P. Insecticidal Efficacy of *Metarhizium anisopliae* Derived Chemical Constituents against Disease-Vector Mosquitoes. *J. Fungi* **2022**, *8*, 300. [CrossRef]
12. Greenfield, B.P.J.; Peace, A.; Evans, H.; Dudley, E.; Ansari, M.A.; Butt, T.M. Identification of *Metarhizium* strains highly efficacious against *Aedes*, *Anopheles* and *Culex* larvae. *Biocontrol Sci. Technol.* **2015**, *25*, 487–502. [CrossRef]
13. Alkhaibari, A.M.; Lord, A.M.; Maffei, T.; Bull, J.C.; Olivares, F.L.; Samuels, R.I.; Butt, T.M. Highly specific host-pathogen interactions influence *Metarhizium brunneum* blastospore virulence against *Culex quinquefasciatus* larvae. *Virulence* **2018**, *9*, 1449–1467. [CrossRef] [PubMed]
14. Knols, B.G.; Bukhari, T.; Arenhorst, M. Entomopathogenic fungi as the next-generation control agents against malaria mosquitoes. *Future Microbiol.* **2010**, *5*, 339–341. [CrossRef] [PubMed]
15. Luz, C.; Mnyone, L.L.; Russell, T.L. Survival of anopheline eggs and their susceptibility to infection with *Metarhizium anisopliae* and *Beauveria bassiana* under laboratory conditions. *Parasitol. Res.* **2011**, *109*, 751–758. [CrossRef]

16. Scheepmaker, J.; Butt, T. Natural and released inoculum levels of entomopathogenic fungal biocontrol agents in soil in relation to risk assessment and in accordance with EU regulations. *Biocontrol Sci. Technol.* **2010**, *20*, 503–552. [[CrossRef](#)]
17. Butt, T.M.; Wood, M.; Taylor, J.W.; Bakirci, S.; Hazir, C.; Ulug, D.; Hazir, S. Differential susceptibility of *Hyalomma excavatum* adults and nymphs to the entomopathogens *Metarhizium anisopliae* ARSEF 4556 and *Steinernema carpocapsae*. *Int. J. Pest Manag.* **2016**, *62*, 261–266. [[CrossRef](#)]
18. Abbott, W.S. A method for computing the effectiveness of an insecticide. *J. Econ. Entomol.* **1925**, *18*, 265–267. [[CrossRef](#)]
19. Hazrat, B.; Ali, S.; Imtinan, A.K. Isolation and efficacy of entomopathogenic fungus *Metarhizium anisopliae* for the control of *Aedes albopictus* Skuse larvae: Suspected dengue vector in Pakistan. *Asian Pac. J. Tropic. Biomed.* **2012**, *2*, 298–300.
20. Haron, E.; Ahmed, M.; Ali, S.; Abas, A.; Elshaiher, M. Evaluate the effects of entomopathogenic fungi isolates on Wheat Aphid, *Schizaphis graminum* (Rondani) (Hemiptera: Aphididae). *Egypt. Acad. J. Biol. Sci. A Entomol.* **2020**, *13*, 149–159. [[CrossRef](#)]
21. Salem, S.S.; Fouda, M.M.; Fouda, A.; Awad, M.A.; Al-Olayan, E.M.; Allam, A.A.; Shaheen, T.I. Antibacterial, cytotoxicity and larvicidal activity of green synthesized selenium nanoparticles using *Penicillium corylophilum*. *J. Cluster Sci.* **2020**, *32*, 351–361. [[CrossRef](#)]
22. Ambika, S.; Gopinath, S.; Saravanan, K.; Sivakumar, K.; Ragupathi, C.; Sukantha, T.A. Structural, morphological and optical properties and solar cell applications of thioglycolic routed nano cobalt oxide material. *Energy Rep.* **2019**, *5*, 305–309. [[CrossRef](#)]
23. Al-Ghamdi, A.A.; Al-Hartomy, O.A.; El Okr, M.; Nawar, A.M.; El-Gazzar, S.; El-Tantawy, F.; Yakuphanoglu, F. Semiconducting properties of Al doped ZnO thin films. *Spectrochim. Acta Part A Mol. Biomol. Spectrosc.* **2014**, *131*, 512–517. [[CrossRef](#)] [[PubMed](#)]
24. Anuradha, C.T.; Raji, P. Facile-synthesis and characterization of cobalt oxide (Co<sub>3</sub>O<sub>4</sub>) nanoparticles by using Arishta leaves assisted biological molecules and its antibacterial and antifungal activities. *J. Mol. Struct.* **2022**, *1262*, 133065. [[CrossRef](#)]
25. Yoo, S.; Lee, E.W.; Kim, D.H. Methane combustion over mesoporous cobalt oxide catalysts: Effects of acid treatment. *Mol. Catal.* **2021**, *511*, 111728. [[CrossRef](#)]
26. Uddin, M.K.; Baig, U. Synthesis of Co<sub>3</sub>O<sub>4</sub> nanoparticles and their performance towards methyl orange dye removal: Characterisation, adsorption and response surface methodology. *J. Clean. Prod.* **2019**, *211*, 1141–1153. [[CrossRef](#)]
27. Gopinath, S.; Mayakannan, M.; Vetrivel, S. Structural, optical, morphological properties of silver doped cobalt oxide nanoparticles by microwave irradiation method. *Ceram. Int.* **2022**, *48*, 6103–6115. [[CrossRef](#)]
28. Yousefi, S.R.; Alshamsi, H.A.; Amiri, O.; Salavati-Niasari, M. Synthesis, characterization and application of Co/Co<sub>3</sub>O<sub>4</sub> nanocomposites as an effective photocatalyst for discoloration of organic dye contaminants in wastewater and antibacterial properties. *J. Mol. Liq.* **2021**, *337*, 116405. [[CrossRef](#)]
29. González-Rubio, G.; Díaz-Núñez, P.; Rivera, A.; Prada, A.; Tardajos, G.; González-Izquierdo, J.; Guerrero-Martínez, A. Femtosecond laser reshaping yields gold nanorods with ultranarrow surface plasmon resonances. *Science* **2017**, *358*, 640–644. [[CrossRef](#)] [[PubMed](#)]
30. Hossain, R.; Sahajwalla, V. Microrecycled Co<sub>3</sub>O<sub>4</sub> from waste lithium-ion battery: Synthesis, characterisation and implication in environmental application. *J. Environ. Chem. Eng.* **2022**, *10*, 107858. [[CrossRef](#)]
31. Purushothaman, K.K.; Sethuraman, B.; Anupama, M.P.; Dhanasankar, M.; Muralidharan, G. Optical, structural, and electrochromic properties of cobalt oxide films prepared via the sol-gel route. *Mater. Sci. Semicond. Processing* **2013**, *16*, 1410–1415. [[CrossRef](#)]
32. Al-Wasidi, A.S.; AlZahrani, I.S.; Thawibaraka, H.I.; Naglah, A.M. Facile synthesis of ZnO and Co<sub>3</sub>O<sub>4</sub> nanoparticles by thermal decomposition of novel Schiff base complexes: Studying biological and catalytic properties. *Arabian J. Chem.* **2022**, *15*, 103628. [[CrossRef](#)]
33. Jadhav, C.H.; Pisal, K.B.; Chavan, A.R.; Patil, S.M.; Patil, P.B.; Pagare, P.K. Electrochemical supercapacitive performance study of spray pyrolyzed cobalt oxide film. *Mater. Today Proc.* **2021**, *43*, 2742–2746. [[CrossRef](#)]
34. Kirthi, A.V.; Rahuman, A.A.; Rajakumar, G.; Marimuthu, S.; Santhoshkumar, T.; Jayaseelan, C.; Velayutham, K. Acaricidal, pediculocidal and larvicidal activity of synthesized ZnO nanoparticles using wet chemical route against blood feeding parasites. *Parasitol. Res.* **2011**, *109*, 461–472. [[CrossRef](#)] [[PubMed](#)]
35. Kainat, K.M.; Ali, F.; Faisal, S.; Rizwan, M.; Hussain, Z.; Zaman, N.; Afsheen, Z.; Uddin, M.N.; Bibi, N. Exploring the therapeutic potential of Hibiscus rosa sinensis synthesized cobalt oxide (Co<sub>3</sub>O<sub>4</sub>-NPs) and magnesium oxide nanoparticles (MgO-NPs). *Saudi J. Biol. Sci.* **2021**, *28*, 5157–5167. [[CrossRef](#)] [[PubMed](#)]
36. Ivask, A.; Titma, T.; Visnapuu, M.; Vija, H.; Kakinen, A.; Sihtmae, M.; Kahru, A. Toxicity of 11 metal oxide nanoparticles to three mammalian cell types in vitro. *Curr. Top. Med. Chem.* **2015**, *15*, 1914–1929. [[CrossRef](#)]
37. Cai, Y.; Wu, D.; Zhu, X.; Wang, W.; Tan, F.; Chen, J.; Qiu, X. Sol-gel preparation of Ag doped MgO nanoparticles with high efficiency for bacterial inactivation. *Ceram. Intern.* **2017**, *43*, 1066–1072. [[CrossRef](#)]
38. Fu, P.P.; Xia, Q.; Hwang, H.M.; Ray, P.C.; Yu, H. Mechanisms of nanotoxicity: Generation of reactive oxygen species. *J. Food Drug Anal.* **2014**, *22*, 64–75. [[CrossRef](#)]
39. Magdolenova, Z.; Collins, A.; Kumar, A.; Dhawan, A.; Stone, V.; Dusinska, M. Mechanisms of genotoxicity. A review of in vitro and in vivo studies with engineered nanoparticles. *Nanotoxicology* **2014**, *8*, 233–278. [[CrossRef](#)]
40. Benelli, G. Plant-mediated synthesis of nanoparticles: A newer and safer tool against mosquito-borne diseases? *Asian Pac. J. Trop. Biomed.* **2016**, *6*, 353–354. [[CrossRef](#)]
41. Foldbjerg, R.; Jiang, X.; Miclăuș, T.; Chen, C.; Autrup, H.; Beer, C. Silver nanoparticles—Wolves in sheep’s clothing. *Toxicol. Res.* **2015**, *4*, 563–575. [[CrossRef](#)]

42. Rai, M.; Kon, K.; Ingle, A.; Duran, N.; Galdiero, S.; Galdiero, M. Broad-spectrum bioactivities of silver nanoparticles: The emerging trends and future prospects. *Appl. Microbiol. Biotechnol.* **2014**, *98*, 1951–1961. [[CrossRef](#)]
43. Jiang, X.; Miclăuş, T.; Wang, L.; Foldbjerg, R.; Sutherland, D.S.; Autrup, H.; Chen, C.; Beer, C. Fast intracellular dissolution and persistent cellular uptake of silver nanoparticles in CHO-K1 cells: Implication for cytotoxicity. *Nanotoxicology* **2015**, *9*, 181–189. [[CrossRef](#)] [[PubMed](#)]
44. Benelli, G. Plant-mediated biosynthesis of nanoparticles as an emerging tool against mosquitoes of medical and veterinary importance: A review. *Parasitol. Res.* **2016**, *115*, 23–34. [[CrossRef](#)] [[PubMed](#)]
45. Alkhaibari, A.M.; Carolino, A.T.; Bull, J.C.; Samuels, R.I.; Butt, T.M. Differential Pathogenicity of *Metarhizium* Blastospores and *Conidia* Against Larvae of Three Mosquito Species. *J. Med. Entomol.* **2017**, *54*, 696–704. [[CrossRef](#)] [[PubMed](#)]
46. Benserradj, O.; Mihoubi, I. Larvicidal activity of entomopathogenic fungi *Metarhizium anisopliae* against mosquito larvae in Algeria. *Int. J. Curr. Microbiol. Appl. Sci.* **2014**, *3*, 54–62.
47. Amóra, S.S.; Bevilaqua, C.M.; Feijó, F.M.; Pereira, R.H.; Alves, N.D.; Freire, F.A.; Kamimura, M.T.; de Oliveira, D.M.; Luna-Alves Lima, E.A.; Rocha, M.F. The effects of the fungus *Metarhizium anisopliae* var. *acridum* on different stages of *Lutzomyia longipalpis* (Diptera: *Psychodidae*). *Acta Trop.* **2010**, *113*, 214–220. [[CrossRef](#)]
48. Alkhaibari, A.M.; Maffeis, T.; Bull, J.C.; Butt, T.M. Combined use of the entomopathogenic fungus, *Metarhizium brunneum*, and the mosquito predator, *Toxorhynchites brevipalpis*, for control of mosquito larvae: Is this a risky biocontrol strategy? *J. Invertebr. Pathol.* **2018**, *153*, 38–50. [[CrossRef](#)]
49. Yee, D.A.; Kesavaraju, B.; Juliano, S.A. Larval feeding behavior of three co-occurring species of container mosquitoes. *J. Vector Ecol.* **2004**, *29*, 315.
50. James, R.; Buckner, J.; Freeman, T. Cuticular lipids and silverleaf whitefly stage affect conidial germination of *Beauveria bassiana* and *Paecilomyces fumosoroseus*. *J. Invertebr. Pathol.* **2003**, *84*, 67–74. [[CrossRef](#)]
51. Mannino, M.C.; Huarte-Bonnet, C.; Davyt-Colo, B.; Pedrini, N. Is the insect cuticle the only entry gate for fungal infection? Insights into alternative modes of action of entomopathogenic fungi. *J. Fungi* **2019**, *5*, 33. [[CrossRef](#)]
52. Subhoshmita, M.; Sibashish, B.; Andras, K.; Gyula, V. Journey of enzymes in entomopathogenic fungi. *Pac. Sci. Rev. A Nat. Sci. Eng.* **2016**, *18*, 85–99.